Aerodynamic Tradeoff Study of Conventional, Canard, and Trisurface Aircraft Systems

Bruce P. Selberg* and Kamran Rokhsaz†
University of Missouri—Rolla, Rolla, Missouri

Conventional, canard, and three-surface aircraft configurations are investigated analytically to determine each configuration's induced and viscous drag under trimmed conditions. A three-surface vortex lattice method is used to trim the aircraft, as well as to predict the induced drag of each configuration. A vortex panel method in conjunction with the momentum integral boundary-layer method is used to predict inviscid and viscous characteristics. Parameters varied including wing to stabilator surface area ratio, static margin, canard to tail loading ratio, and $C_{L_{trim}}$. For all of the parameters considered, the conventional configuration had the highest $C_{L_{trim}}/C_{Di}$. At the lower stabilator aspect ratios, the $C_{L_{trim}}/C_D$ of the conventional aircraft was the highest, whereas for the highest stabilator aspect ratio considered the canard configuration had the highest $C_{L_{trim}}/C_D$. The trisurface was superior to the canard at the lower aspect ratio with the canard becoming superior at the higher values.

Nomenclature

a.c. = aerodynamic center
$\mathcal{R}$ = aspect ratio
c.g. = center of gravity
$\bar{C}$ = wing average chord
C_d = sectional drag coefficient
C_{Di} = induced drag coefficient
C_D = total drag coefficient
C_l = sectional lift coefficient
C_{ℓ_α} = two-dimensional lift curve slope
C_L = total lift coefficient
C_{L_α} = total lift curve slope
C_{L_δ} = $\partial C_L/\partial\delta$ = variation of lift coefficient with control surface deflection
C_M = pitching moment coefficient
C_{M_α} = $\partial C_M/\partial\alpha$ = variation of pitching moment coefficient with aircraft angle of attack
C_{M_δ} = $\partial C_M/\partial\delta$ = variation of pitching moment coefficient with control surface deflection
C_{M_0} = total pitching moment coefficient at zero lift
L/D = total lift-to-drag ratio
q_∞ = freestream dynamic pressure
R_c = Reynolds number based on chord
S = area
V = velocity
W/S = wing loading
Wt = weight
X = moment arm
$\bar{X}$ = distance divided by the wing chord
α = airplane angle of attack
λ = taper ratio
δ = control surface deflections

Subscripts

c = canard
t = horizontal tail
w = wing

Received Sept. 26, 1985; presented as Paper 85-4071 at the AIAA 3rd Applied Aerodynamics Conference, Colorado Springs, CO, Oct. 14-17, 1985; revision received May 7, 1986. Copyright © American Institute of Aeronautics and Astronautics, Inc., 1986. All rights reserved.

*Professor of Aerospace Engineering, Mechanical and Aerospace Engineering Department. Associate Fellow AIAA.

†Teaching Fellow, Mechanical and Aerospace Engineering Department. Member AIAA.

Introduction

OVER the past several years interest in nonconventional airplane configurations has markedly increased. Canard configurations have received most of the attention, with Rutan[1,2] starting this interest for nonmilitary applications with several successful canard configurations. The most recent canard additions are the Avtek and Beech's Starship I. All of the successful canard aircraft have demonstrated stall proof characteristics. Several authors have studied the minimum induced drag of both tail aft configurations and canard configurations. Nayor[3] and Laitone[4-6] have used the theories developed by Prandtl[7,8] and Munk[9,10] to study the minimum induced drag of two-surface aircraft. McLaughlin[11] and Keith and Selberg[12] have both compared canard and conventional configurations analytically and found that canard configurations have lower flight efficiencies than tail aft configurations when each are trimmed for similar static margins. This is caused by the high canard loading that is required for trim in the canard aircraft.

Recently, renewed interest has centered around the three-surface aircraft: a canard, a wing, and an aft tail. Kendall[13] has presented an analysis based on Prandtl/Munk theories to predict minimum induced drag for these three-surface aircraft, specifically the Gates-Piaggio GP-180. Kendall's results indicate that the induced drag of the three-surface configurations can ideally be lower than either the conventional or canard configuration. His analysis assumes elliptical lift distribution, as do all of the other above results that utilize the Prandtl/Munk method. However, in addition, the Munk stagger theorem requires that as the various lifting surfaces are moved longitudinally to obtain trim, the relative lift between these various surfaces remains the same as the stagger changes. As stagger changes, the two-dimensional aerodynamic coupling causes the C_{ℓ_α} of both ther canard, wing, and/or tail to change, thus requiring changes in the angle of attack of these surfaces to maintain the same relative lift as specified by the Munk stagger theorem. Keith and Selberg[12] have shown that as both stagger and gap increase, the coupling decreases. Thus, as stagger increases the angle of attack between the two surfaces, the decalage angle must increase to keep the same relative lift. However, as decalage angle increases, the drag increases significantly. For a lift coefficient of 0.4 with the MS(1)-0313 airfoil at a Reynolds number of 2×10^6, a change in decalage angle from 0.0 to 4.0 increases the viscous drag by 36%.

The purpose of this paper is to analyze conventional wing/tail, canard/wing, and three-surface, canard/wing/tail

configurations with common fuselage and vertical tail. Both the two- and three-dimensional drags will be calculated under typical cruise conditions. The NASA MS(1)-0313 medium-speed airfoil will be used for all lifting surfaces.

The primary objective of the study will be to analyze the behavior of the ratio $C_{L_{\text{trim}}}/C_{Di}$ over a range of static margins and area ratios.

Method of Analysis

Three-Dimensional Analysis

Three-dimensional results were predicted with a three-surface vortex lattice program. This program has two versions: the two-dimensional coupled version for small staggers and the two-dimensional uncoupled version for large staggers. Rokhsaz and Selberg[14] have shown that for large staggers, like those considered in this paper, the two-dimensionally uncoupled version provides essentially the same results as the coupled version. The uncoupled version, which uses uncoupled C_{ℓ_α} and C_{ℓ_0} airfoil data as input, will be used for this study. Many authors[15-17] use variations of the Munk analysis for induced drag calculations. None of these methods accounts for either airfoil thickness or the deformation of the spanwise lift distribution as the result of three-dimensional coupling.

Figure 1 illustrates the degree of agreement of the UMR vortex lattice program, which included thickness effects, with a wing fuselage NASA model after Paulson[18] with a $\mathcal{R}=8.98$. There is excellent agreement up to the beginning of boundary-layer separation.

Two-Dimensional Analysis

The two-dimensional analysis utilized a multielement vortex panel program[19] where the airfoils were approximated by polygons. The inviscid multielement program was joined to a momentum integral boundary-layer analysis program to compute theoretical two-dimensional viscous data. The laminar flow portion of the momentum integral program predicted the behavior of the boundary layer with Thwaites' method[20] and used Michel's transition criterion[21] to determine the transition points. The turbulent flow solution was then obtained by the method of Head and Cumpsty[22] and the viscous drag was calculated with the Squire-Young formula.[23] Viscous drag predictions using the combined vortex panel boundary-layer program were compared to experimental results known at the same Reynolds numbers to determine the degree of correlation between experimental and analytical results. Figure 2 shows the theoretical and the experimental data[24] for the MS(1)-0313 airfoil at a Reynolds number R_c of 6×10^6. This good agreement was achieved by using a factor of 2.2 for the MS(1)-0313 in the Squire-Young equation. Similar good results were obtained at other Reynolds numbers.

Stability and Control

Each configuration was trimmed using multielement vortex lattice program. Component weights, component center-of-gravity location, location of each lifting surface, etc., were all input quantities for the vortex lattice stability and control program. Once the lift of the various lifting surfaces was calculated from the vortex lattice program, then the total lift and pitching moment coefficients were determined from

$$C_L = C_{L_w} + C_{L_c}\left(\frac{S_c}{S_w}\right) + C_{L_t}\left(\frac{S_t}{S_w}\right) \tag{1}$$

and

$$C_M = C_{M_{0_{wB}}} - C_{L_w}\left(\frac{X_w}{\bar{C}}\right) - C_{L_c}\left(\frac{X_c S_c}{\bar{C} S_w}\right) - C_{L_t}\left(\frac{X_t S_t}{\bar{C} S_w}\right) \tag{2}$$

where the airfoil placement and moment arm definitions are shown in Fig. 3. Small perturbations were introduced in the incidence angles of the airplane, the canard, and the tail in order to calculate the longitudinal stability derivatives. The lift and pitching moment coefficients can also be expressed as

$$C_L = C_{L_\alpha}\alpha + C_{L_{\delta_c}}\delta_c + C_{L_{\delta_t}}\delta_t \tag{3}$$

$$C_M = C_{M_0} + C_{M_\alpha}\alpha + C_{M_{\delta_c}}\delta_c + C_{M_{\delta_t}}\delta_t \tag{4}$$

Furthermore, under trim conditions,

$$C_L = C_{L_{\text{trim}}} = W_t/q_\infty S_w$$

and

$$C_M = 0$$

Knowing the longitudinal stability derivatives and using the trim conditions, Eqs. (3) and (4) can be solved for α_{trim}, $\delta_{c_{\text{trim}}}$, and $\delta_{t_{\text{trim}}}$.

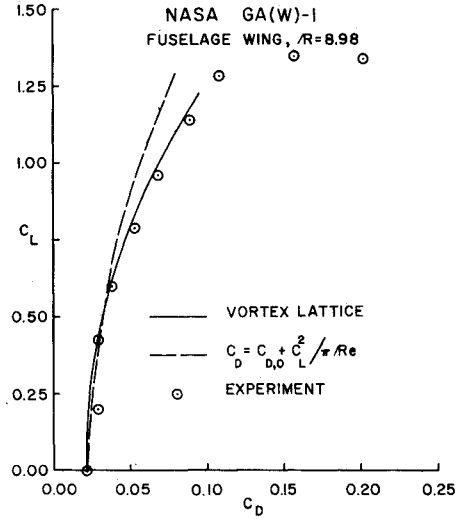

Fig. 1 Comparison of vortex lattice program with experimental results.

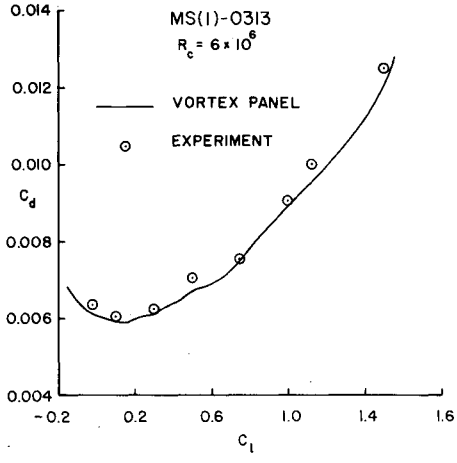

Fig. 2 Two-dimensional MS(1)-0313 drag polar.

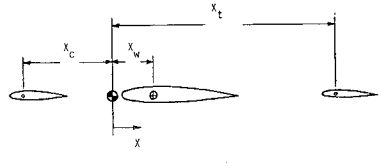

Fig. 3 Wing and stabilator surface nomenclature.

$$\alpha_{\text{trim}} = \frac{C_{L_{\text{trim}}} - C_{L_{\delta_c}}\delta_{c_{\text{trim}}} - C_{L_{\delta_t}}\delta_{t_{\text{trim}}}}{C_{L_\alpha}} \tag{5}$$

and

$$\left[C_{M_{\delta_c}} - C_{M_\alpha}\left(\frac{C_{L_{\delta_c}}}{C_{L_\alpha}}\right)\right]\delta_{c_{\text{trim}}} + \left[C_{M_{\delta_t}} - C_{M_\alpha}\left(\frac{C_{L_{\delta_t}}}{C_{L_\alpha}}\right)\right]\delta_{t_{\text{trim}}} + C_{M_\alpha}\left(\frac{C_{L_{\text{trim}}}}{C_{L_\alpha}}\right) + C_{M_0} = 0 \tag{6}$$

For both the canard and conventional cases, some of the stability derivatives are zero, namely $C_{M_{\delta_t}}$ and $C_{L_{\delta_t}}$ for the former and $C_{M_{\delta_c}}$ and $C_{L_{\delta_c}}$ for the latter. For the trisurface case, an additional equation is required for a unique solution. This equation

$$C_{L_c}S_c/C_{L_t}S_t = B \tag{7}$$

where B is the loading constant. For equal canard and tail loads, B will be -1.0. The trisurface case is solved using that value of B resulting in the largest C_L/C_{Di}.

Flight Specifications

The three configurations, conventional, wing/tail, canard/wing, and canard/wing/tail, were compared for a six-place 1200 lb payload configuration. The configurations each had a common fuselage and vertical tail and met the specifications shown in Table 1.

Table 1 Flight specifications

Class	Six-place business aircraft
Payload	1200 lbf
Max. gross weight	4600 lbf (approx.)[a]
S_w	120 ft^2
AR_w	12
$AR_c = AR_t$	9
$\lambda_w = \lambda_c = \lambda_t$	0.8
$C_{L_{\text{trim}}}$	0.23 (approx.)[b]
Lifting surface	NASA MS(1)-0313
Scaled P&W PT6-45A turboprop with pusher propeller[25]	

[a]Obtained from estimates for an advanced technology design.[26] [b]Corresponding to $V = 500$ ft/s at 20,000 ft altitude.

Reference 26 was used as a guide in determining these constraints. Wing weight was estimated according to the NASTRAN verified method of Refs. 27 and 28, while the fuselage and the payload weights were directly extracted from Ref. 27. Aspect ratios were limited such that they would be feasible for all-composite lifting surfaces. The three configurations are shown in Figs. 4-6. Figure 4 is the conventional wing/aft tail aircraft. The six-place canard is shown in Fig. 5 and the trisurface six-place in Fig. 6.

The computer code was arranged so that it would also estimate the longitudinal stability derivatives of the aircraft necessary for trim. All aircraft were trimmed assuming all-moving tail or canard, whichever was applicable. For trisurface aircraft, the incidence angle of the canard was assumed to be known a priori and trim was achieved by moving the tail. Once trim was established, the induced drag of the entire configuration could be calculated.

Using the above equations each aircraft configuration was trimmed. For the trisurface, a search was performed for the relative loads of the two surfaces that would result in the largest value of $C_{L_{\text{trim}}}/C_{Di}$ for the entire aircraft. The results of such process are shown in Fig. 7 for a typical value of the

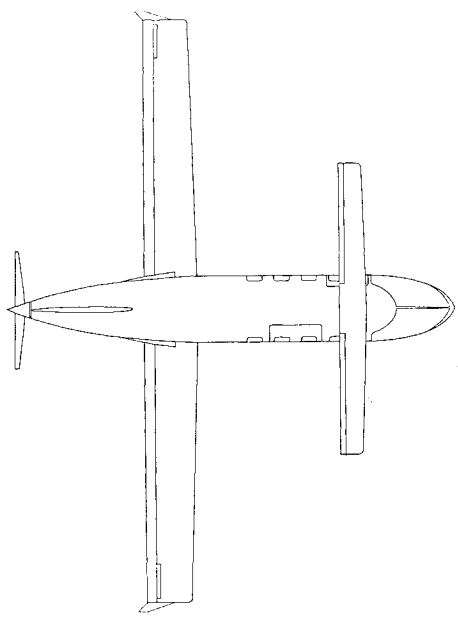

Fig. 5 Top view of six-place canard configuration.

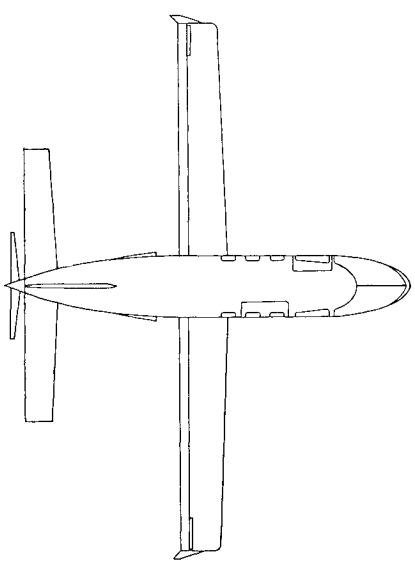

Fig. 4 Top view of six-place conventional configuration.

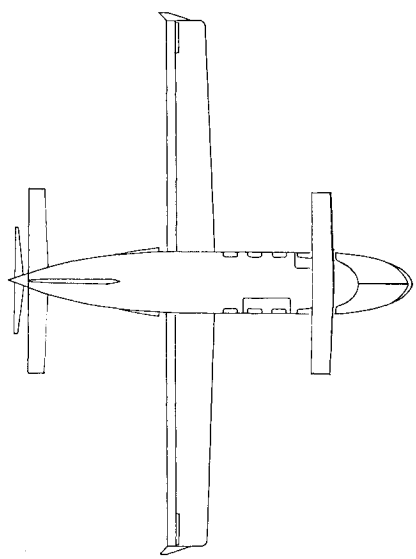

Fig. 6 Top view of six-place trisurface configuration.

area ratio at several static margins. Area ratio here is defined as the ratio of the wing area to the sum of the tail and canard areas. C_L/C_{Di} increases as static margin decreases.

The maximum value of C_L/C_{Di} occurs at approximately a canard to negative tail load of 2.0. The degradation in C_L/C_{Di} is not as severe at the higher canard to tail loadings as it is at canard to tail loading below 2.0. Similar trends were observed for other area ratios. Variations in static margin were obtained by moving the wing while holding the area ratio fixed. Different area ratios were obtained by changing the sizes of the canards and the horizontal tails with constant aspect ratio of 9. For the trisurface cases, equal areas were used for the canard and the tail.

Figure 8 shows the effects of static margin and tail size on C_L/C_{Di}. The C_L/C_{Di} illustrates the same trends with static margin; however, the numerical changes are greater. Increases in the tail size also increases C_L/C_{Di} because of the lower C_L of the tail and, hence, the lower induced drag.

C_L/C_{Di}, for the canard, is shown in Fig. 9 as a function of static margin and canard area. The same static margin trends occur here as did for the convention and trisurface configurations. However, the changes in C_L/C_{Di} for a large range of static margin change are much less. Similarly, the largest area

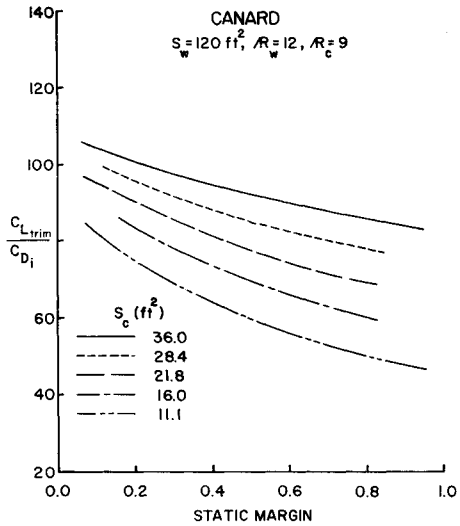

Fig. 9 Canard configuration induced drag sensitivity with changes in static margin and canard area.

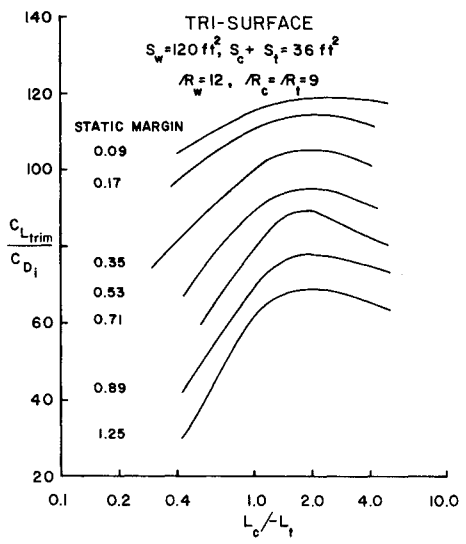

Fig. 7 Trisurface induced drag sensitivity to the ratio of canard-to-tail loading and static margin.

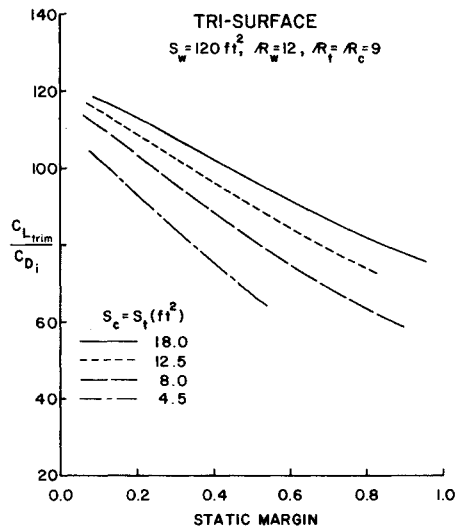

Fig. 10 Trisurface induced drag sensitivity with changes in static margin and stabilator surface areas.

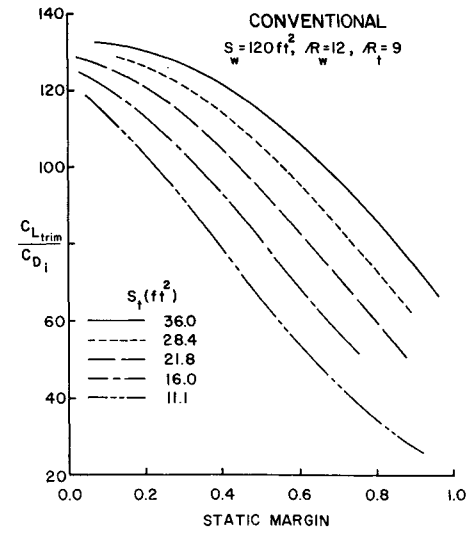

Fig. 8 Conventional configuration induced drag sensitivity with changes in static margin and tail area.

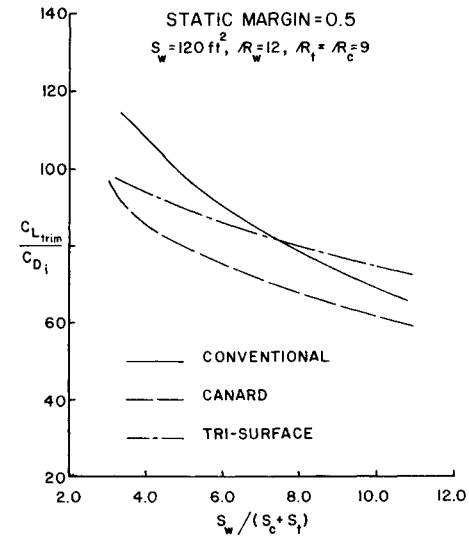

Fig. 11 Induced drag summaries with changes in ratio of wing area to stabilator area for a static margin of 0.5.

canard has the least induced drag and, hence, the highest C_L/C_{Di}.

Results for the trisurface aircraft are shown in Fig.10 as a function of static margin and canard/tail area. This figure represents the optimum C_L/C_{Di} for each combination of area ratio and static margin. It was obtained by constructing plots similar to Fig. 7 for every combination of area ratios and static margins and then extracting the optimum values for each of these combinations. The variation in C_L/C_{Di} for the trisurface lies between those of the conventional and the canard. As before the largest area/least loaded surfaces have the highest C_L/C_{Di}.

Figure 11 represents the C_L/C_{Di} as a function of area ratios at a static margin of 0.5. The highest C_L/C_{Di} occurs at the lowest ratio of the wing to canard-plus-tail area. In this lowest area region, the conventional configuration performs the best, followed by the trisurface and then by the canard. In Fig. 11, the trisurface appears to be more efficient for area ratios greater than 7.5. However, in that range, the very small surface areas of the tail and the canard require that very high lift coefficients be generated by these surfaces. This greatly limits the effective range of $C_{L_{trim}}$.

Figure 12 illustrates the C_L/C_{Di}, for a static margin of 0.2, as a function of area ratio. Again, the conventional configuration is superior, followed by the trisurface and then the canard. This order holds for all area ratios.

These results are summarized in Fig. 13 for $\mathcal{R}_w = 12$ and $\mathcal{R}_c = \mathcal{R}_t = 9$, over a range of static margins for the smallest (i.e., the most efficient) area ratio considered in the research. As demonstrated here, the trisurface aircraft remains inferior, from induced drag considerations, to conventional geometries for static margins less than 0.85. On the other hand, for larger static margins, it is the canard configuration that has the highest C_L/C_{Di}. For a typical series of business jets, the static margin varies from 0.25 to 0.43 at the forward c.g. limits. This is not even close to the crossover point of 0.8 in Fig. 13.

If different flight velocities and/or altitudes are considered and the configurations are again analyzed for a static margin of 0.2, Fig. 14 is the result. Here, $C_{L_{trim}}/C_{Di}$ is shown vs $C_{L_{trim}}$. Again, the conventional is superior for all trim lift coefficients, followed by the trisurface and the canard. The efficiency factor e, which is

$$e = C^2_{L_{trim}}/C_{D_i}\pi\mathcal{R}$$

is plotted in Fig. 15 for the case just discussed in Fig. 14. This is just another way of visualizing the results of Fig. 14. Adding the viscous and pressure drag from the vortex panel/momentum boundary-layer programs to the above cases produces the results in Fig. 16. The general trends remain unchanged. The conventional still has the highest performance with the trisurface and canard lower in that order.

Feistel[29] has used a Prandtl-Munk analysis to study various parameters such as span, gap, aspect ratio, etc. His results indicated that a $\mathcal{R}_c/\mathcal{R}_w$ of 1.5–2.0 was necessary to achieve peak span efficiences. In order to assess these results, the canard and tail aspect ratios were varied for the original configurations under the remaining conditions of Table 1. The loading ratio L_c/L_t was held constant at the previously obtained optimum of -2.0. Figure 17 shows the results of these calculations in terms of $C_{L_{trim}}/C_{Di}$ vs aspect ratio ratio ($\mathcal{R}_c/\mathcal{R}_w = \mathcal{R}_t/\mathcal{R}_w$) for a static margin of 0.2. On the other hand, the canard experiences a 30% improvement in $C_{L_{trim}}/C_{Di}$. Figure 18 shows the efficiency factor for this case vs aspect ratio ratio. As would be expected, the same trends

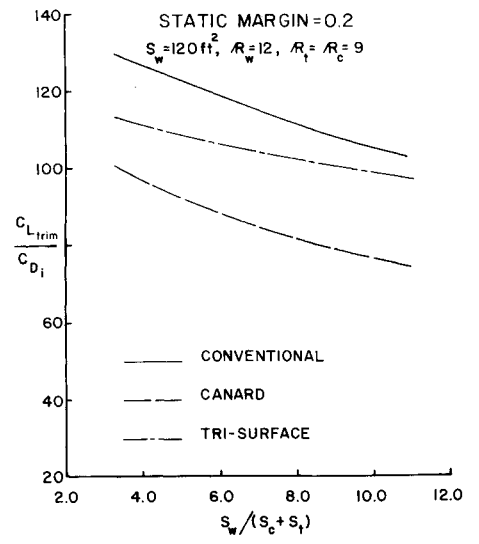

Fig. 12 Induced drag summaries with changes in ratio of wing area to stabilator area for a static margin of 0.2.

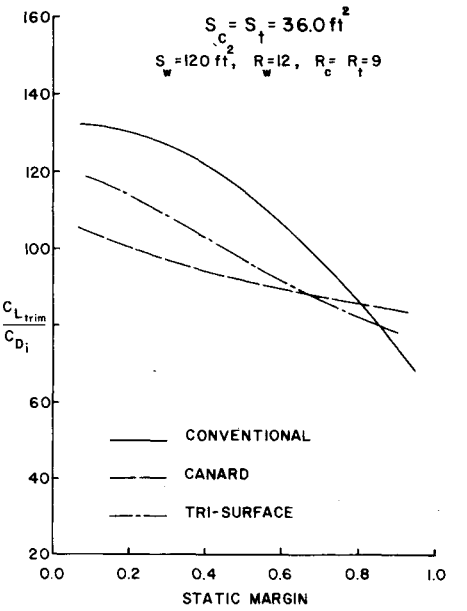

Fig. 13 Induced drag summaries with changes in static margin.

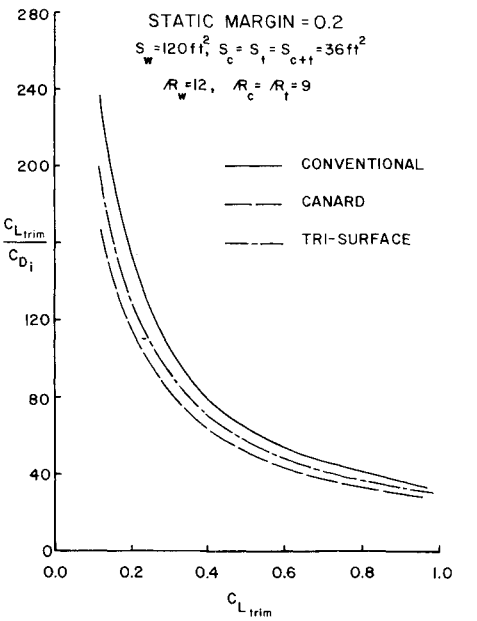

Fig. 14 Configurational induced drag variations with trim lift coefficient.

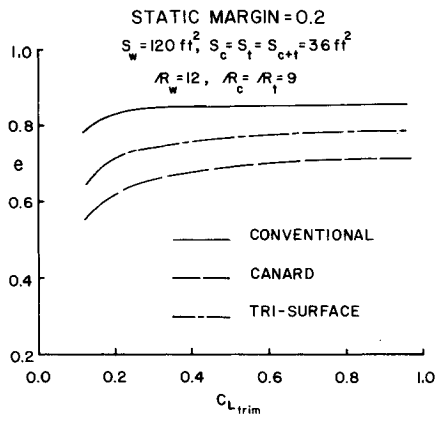

Fig. 15 Configurational efficiency factor comparison.

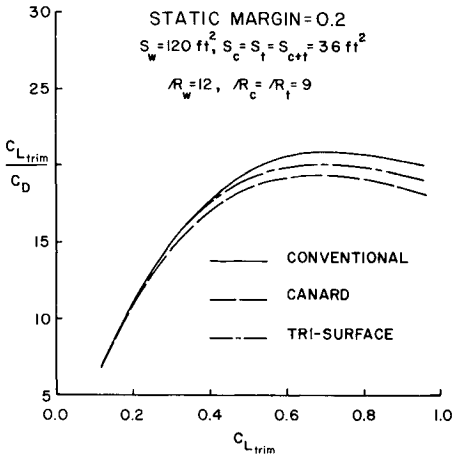

Fig. 16 Overall lift-to-drag comparisons.

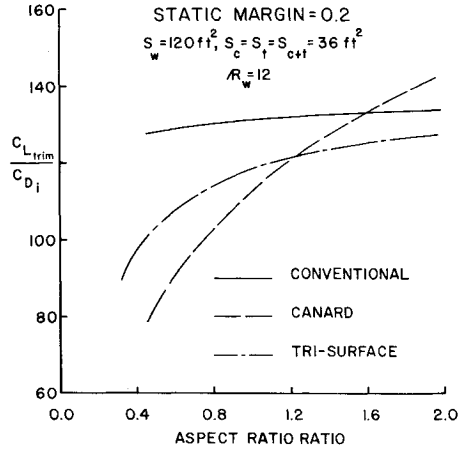

Fig. 17 Changes in induced drag with the ratio of canard and/or tail $\mathcal{R}$ to wing $\mathcal{R}$.

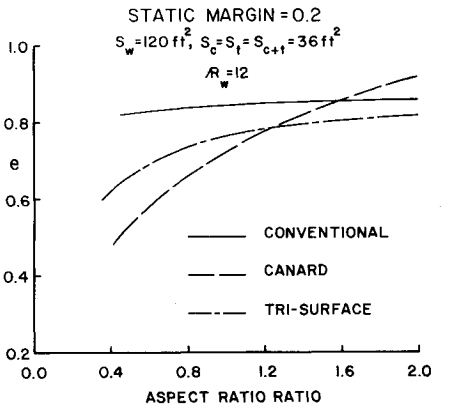

Fig. 18 Configurational efficiencies with changes in the ratio of canard and/or tail $\mathcal{R}$ to wing $\mathcal{R}$.

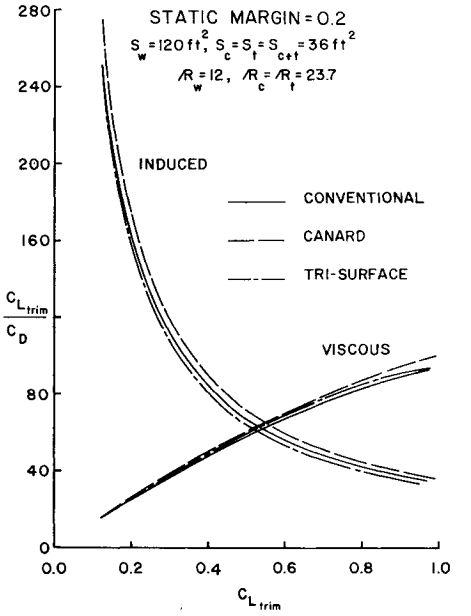

Fig. 19 Induced and viscous drag coefficient variations with trim lift coefficient for $\mathcal{R}_s/\mathcal{R}_w$ of 2.0.

exist. If the optimum loading ratio had been searched for in Figs. 17 and 18, then as the aspect ratio of the canard and/or tail to wing aspect ratio increased, the $C_{L_{trim}}/C_{Di}$ of the trisurface probably would have trends higher than those shown in the two figures. However, even in the limit when the canard is to carry all of the load, the tail will still produce significant induced drag due to the flowfield deformation in the wake of the canard and wing. Induced drag and viscous drag results for canard aspect ratio to wing aspect ratio of 2.0 are plotted in Fig. 19 for a static margin of 0.2. For these conditions, the canard is superior from both induced and viscous drag considerations. The conventional is next best for induced drag, but worst in viscous drag. That leaves the trisurface worst from induced drag considerations and second in viscous drag. When pressure and viscous drags are added to the induced drag of Fig. 19, then Fig. 20 is obtained for $C_{L_{trim}}/C_D$ vs $C_{L_{trim}}$. The $C_{L_{trim}}/C_D$ of the canard is the highest, followed by the conventional and then the trisurface. The aspect ratio of the canard and tail at 23.7 are not practical because of structural and aeroelastic problems. However, these same trends would occur for canard and tail aspect ratios of 14.0 with wing aspect ratios around 7 and 8. Viscous runs were made for the natural laminar flow, NASA NLF-0215F, and NACA 23012 airfoils. The NLF results raised the overall $C_{L_{trim}}/C_D$ results shown in Fig. 20, whereas the 23012 airfoil lowered the results from those shown in Fig. 20.

The input geometry constraints could have an effect on the results. For the trisurface aircraft, the area of the canard and tail were kept equal. If these areas were allowed to change, keeping their total area the same as the trim surface areas of the canard or conventional configurations, then the above trends might be somewhat changed. For instance, as the area of the canard becomes larger with tail area getting smaller while concurrently keeping the same total area, then the results will approach those of the canard. Likewise, if the

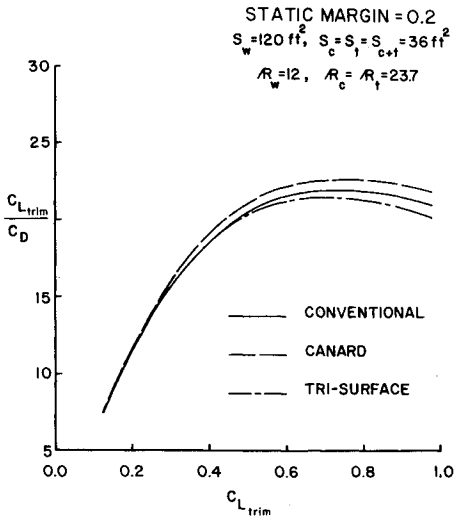

Fig. 20 Overall lift-to-drag comparisons for $\mathcal{R}_s/\mathcal{R}_w$ of 2.0.

aspect ratio of the trimming surfaces for any one of the three configurations was allowed to differ from the other two, different results would occur. However, this would be an unfair comparison for whichever configuration had the lower aspect ratios. The gaps for the canard to wing were about 2.0 nondimensionalized with respect to the wing chord. The gaps between the wing and horizontal tail were close to zero measured in the same manner. However, the effect of gap was negligible because of the large stagger between the lifting and/or trimming surfaces.

Conclusion

Conventional, canard, and trisurface aircraft were analytically studied for a typical six-place business aircraft to determine their induced, viscous, and pressure drag. The parameters varied included the static margin, stabilator surface area, stabilator loading ratios, and aspect ratio. The highest stabilator surface areas produced the least induced drag for all configurations. At normal static margins and lower stabilator aspect ratios, the canard has the highest induced drag, followed by the trisurface and then the conventional. However, when viscous drag is included, then conventional configuration has the highest lift-to-drag ratio, followed by the trisurface and the canard. At the higher stabilator aspect ratios, the canard has the least induced drag as well as the highest $C_{L_{trim}}/C_D$ ratio. The conventional configuration is second, followed by the trisurface. However, in all cases, the overall $C_{L_{trim}}/C_D$ is close enough that configuration selection will most probably be based on other considerations, i.e., stability and control, safety, structures, manufacturing costs, etc.

References

[1]Rutan, B., "Development of Small High-Aspect-Ratio Canard Aircraft," *The Society of Experimental Test Pilots*, Vol. 15, No. 2, 1980.

[2]Rutan, B., "Tale of the Three EZ's," *Sport Aviation*, Vol. 29, No. 2, Feb. 1980.

[3]Nayor, C. H., "Notes on the Induced Drag of a Wing-Tail Combination," British Aeronautical Research Council, R&M 2528, 1954.

[4]Laitone, E. V., "Ideal Tail Load for Minimum Aircraft Drag," *Journal of Aircraft*, Vol. 15, March 1978.

[5]Laitone, E. V., "Positive Tail Loads for Minimum Induced Drag of Subsonic Aircraft," *Journal of Aircraft*, Vol. 15, Dec. 1978.

[6]Laitone, E. V., "Prandtl's Bi-Plane Theory Applied to Canard and Tandem Aircraft," *Journal of Aircraft*, Vol. 17, April 1980.

[7]Prandtl, L., "Applications of Modern Hydrodynamics To Aeronautics," NACA Rept. 116, 1921.

[8]Prandtl, L., "Induced Drag of Multi-Planes," NACA TN, 182, 1924.

[9]Munk, M. M., "The Minimum Induced Drag of Aerofoils," NACA Rept. 121, 1921.

[10]Munk, M. M., "General Bi-Plane Theory," NACA Rept. 151, 1922.

[11]McLaughlin, M. D., "Calculations and Comparison with an Ideal Minimum of Trimmed Drag for Conventional and Canard Configurations Having Various Levels of Static Stability," NASA TN D-8391, May 1977.

[12]Keith, M. W. and Selberg, B. P., "Aerodynamic Optimization, Comparison, and Trim Design of Canard and Conventional High Performance General Aviation Configurations," AIAA Paper 83-0058, Jan. 1983.

[13]Kendall, E. R., "The Minimum Induced Drag, Longitudinal Trim and Static Longitudinal Stability of Two-Surface and Three-Surface Airplanes," AIAA Paper 84-2164, Aug. 1984.

[14]Rokhsaz, K. and Selberg, B. P., "Analytical Study of Three-Surface Lifting Systems," SAE Paper 850866, April 1985.

[15]Laitone, E. V., "Prandtl's Biplane Theory Applied to Canard and Tandem Aircraft," *Journal of Aircraft*, Vol. 17, April 1980, pp. 233-237.

[16]Kroo, I. M., "Minimum Induced Drag of Canard Configurations," *Journal of Aircraft*, Vol. 19, Sept. 1982, pp. 792-794.

[17]Butler, G. F., "Effect of Downwash on the Induced Drag of Canard-Wing Combinations," *Journal of Aircraft*, Vol. 19, May 1982, pp. 410-411.

[18]Paulson, J. W., "Application of Vortex Lattice Theory to Preliminary Aerodynamic Design," NASA Rept., 1976.

[19]Rokhsaz, K., "Analytical Investigation of the Aerodynamic Characteristics of Dual Wing Systems," M.S. Thesis, University of Missouri, Rolla, 1980.

[20]Thwaites, B., "Approximate Calculation of the Laminar Boundary Layer," *Aeronautical Quarterly I*, 1949.

[21]Michel, R., "Etude de la Transition sur les Profiles d'Aile; Establissement d'un Critere de Determination de Point de Transition et Calcul de la Trainee de Profile Incompressible," ONERA Rept. 1/1578A, 1951.

[22]Dvorak, F. A. and Woodward, F. A., "A Viscous/Potential Flow Interaction Analysis Method for Multi-Element Infinite Swept Wings, Vol. I," NASA CR-2476, 1974.

[23]Cebeci, T. and Smith, A. M. O., "Calculation of Profile Drag of Airfoils at Low Mach Numbers," *Journal of Aircraft*, Vol. 5, Nov.-Dec. 1968, pp. 535-542.

[24]McGhee, R. J., "Wind Tunnel Results for a 13-Percent-Thick Medium Speed Airfoil Section," NASA TM, to be published.

[25]Holmes, B. J. and Croom, C. C., "Aerodynamic Design Data for a Cruise-Matched High Performance Single Engine Airplane," SAE Paper 810625, 1981.

[26]Keith, M. W. and Selberg, B. P., "Aerodynamic Design Optimization/Trim Analysis of Canard/Conventional Configurations," *Journal of Aircraft*, Vol. 21, March 1983, pp. 183-192.

[27]Keith, M. W., "Parametric Canard/Wing Aerodynamic Trade-Off Analysis and Design Comparison of Canard and Conventional High Performance General Aviation Configurations," M.S. Thesis, University of Missouri, Rolla, 1982.

[28]Somnay, R. J., "Design of Dual Wing Structures," M.S. Thesis, University of Missouri, Rolla, 1983.

[29]Feistel, T. W., "Interdependence of Parameters Important to the Design of Subsonic Canard-Configured Aircraft," SAE Paper 850865, April 1985.